

## Control of charge order melting through local memristive migration of oxygen vacancies

Zhi-Hong Wang,<sup>1,\*</sup> Q. H. Zhang,<sup>1</sup> G. Gregori,<sup>2</sup> G. Cristiani,<sup>2</sup> Y. Yang,<sup>3</sup> X. Li,<sup>4</sup> L. Gu,<sup>1,5</sup>  
J. R. Sun,<sup>1</sup> B.-G. Shen,<sup>1</sup> and H.-U. Habermeier<sup>2</sup>

<sup>1</sup>Beijing National Laboratory for Condensed Matter Physics, Institute of Physics, Chinese Academy of Sciences, Beijing 100190, China

<sup>2</sup>Max Planck Institute for Solid State Research, Heisenbergstrasse 1, D-70569, Stuttgart, Germany

<sup>3</sup>General Research Institute for Nonferrous Metals, 2 Xijiekou Wai, Beijing 100088, China

<sup>4</sup>School for Materials Science and Engineering, Beijing Institute of Technology, Beijing 10081, China

<sup>5</sup>Collaborative Innovation Center of Quantum Matter, Beijing 100190, China



(Received 9 November 2017; published 21 May 2018)

The colossal magnetoresistance (CMR) in perovskite manganites and the resistive switching (RS) effect in metal-oxide heterostructures have both attracted intensive attention in the past decades. Up to date, however, there has been surprisingly little effort to study the CMR phenomena by employing a memristive switch or by integrating the CMR and memristive properties in a single RS device. Here, we report a memristive control of the melting of the antiferromagnetic charge ordered (AFM-CO) state in  $\text{La}_{0.5}\text{Ca}_{0.5}\text{MnO}_{3-\delta}$  epitaxial films. We show that an *in situ* electro-tailoring of the boundary condition, which results in layers of oxygen vacancies at the metal-oxide interface, can not only suppress the critical magnetic field for the AFM-CO state melting in the interfacial memristive domain, but also promote the one in the common pristine domain of the RS device in the high and low resistive states. Our study thereby highlights the pivotal roles of functional oxygen vacancies and their dynamics in strong correlation physics and electronics.

DOI: [10.1103/PhysRevMaterials.2.054412](https://doi.org/10.1103/PhysRevMaterials.2.054412)

### I. INTRODUCTION

Perovskite manganites have long been a focus of condensed matter physicists and material scientists due to the colossal magnetoresistance (CMR) and the strong correlation physics involved in these transition metal oxides. Of particular interest are the manganites near half-doping, in which spin, charge, and orbital can be cooperatively ordered, and the magnetic-field-induced transition from antiferromagnetic (AFM) charge-orbital ordered (CO) insulator to ferromagnetic (FM) metal generally leads to typical CMR with resistivity changed up to several orders of magnitude [1,2]. Since the so-called charge-exchange-type CO phase was unveiled by the seminal works of Wohlan, Koehler, and Goodenough [3,4], nontrivial physical states continue being discovered or theoretically assessed in these materials, such as charge order within FM domains [5], electronically soft phases [6,7], sliding charge-density wave [8], and orbital solitons [9,10]. Meanwhile, in addition to magnetic field [2], electric field [11] and photoirradiation [12–16] have been employed to induce striking insulator to metal transitions below the CO temperature. Despite these efforts and achievements, many aspects of the AFM-CO states remain to be elucidated owing to the entangled spin, charge, and lattice degrees of freedom.

One critical issue of both fundamental and technological relevance is how readily the AFM-CO state melting can be tuned with internal and/or environmental parameters. In  $\text{Nd}_{0.5}\text{Ca}_{0.5}\text{MnO}_3$ ,  $\text{Nd}_{1-x}\text{Sr}_x\text{MnO}_3$ , and  $\text{Pr}_{1-x}\text{Ca}_x\text{MnO}_3$  ( $0.4 < x \leq 0.5$ ), for example, there exhibit robust CO states,

for which the photoinduced melting is difficult to achieve [12,15]. Regarding magnetic perturbations, the critical field for AFM-CO state melting can be very high even up to  $\sim 60$  T in some half-doped manganites [1]. To explore the melting efficiency, recent attempts have been made in the manganites of statically or dynamically weakened CO states, noting that Mott insulators with a short-range charge order tend to have the AFM-CO matrix embedded with charge disordered FM clusters, and the latter can be precursors to promote the AFM-CO state melting [17]. For instance, in  $(\text{La}_{1-x}\text{Y}_x)_{0.5}(\text{Ca}_{1-y}\text{Sr}_y)_{0.5}\text{MnO}_3$ , we have shown that the cation disorder destabilizes the  $d_{3x^2-r^2}/d_{3y^2-r^2}$  orbital stripe alternation through suppressing the orthorhombicity in the *ab* plane, which causes spin nematicity and thereby lowers the magnetic field required for melting the AFM-CO state [18]. More recently, the destruction of crystal anisotropy either in  $\text{Gd}_{0.55}\text{Sr}_{0.45}\text{MnO}_3$  with cation disorder, or in  $\text{Pr}_{0.6}\text{Ca}_{0.4}\text{MnO}_3$  by double laser pulses, has also been proved to enhance the melting of the AFM-CO state [13,14,16].

Apart from introducing cation disorder, oxygen vacancy doping is an alternative approach for tuning the AFM-CO states. However, systematic oxygen reduction through vacuum annealing is time consuming and, in fact, a precise control of oxygen vacancies in oxides remains an experimental challenge [19–21]. Recently, the resistive switching (RS) effect in metal-oxide-metal heterostructures has attracted extensive attention and the working principle is known to rely on the local electromigration of oxygen vacancies [22–28]. For the RS devices based on perovskite oxides, there generally occurs the interface-type memristive switching, i.e., resistance changes due to oxygen vacancies motion at the metal-oxide interface [26]. Compared to the magnetoelectric control at

\*Corresponding author: z.wang@iphy.ac.cn

heterointerfaces [29–31], the interface-type oxygen vacancies motion in RS devices should provide a more direct *in situ* scheme to tailor the strongly correlated behavior in perovskite oxides. Up to this date, although the practice was reported to tune the magnetic states in  $\text{SrCoO}_{3-\delta}$  [32], there has been surprisingly little effort to study the CMR phenomena by employing a memristive switch or by integrating the CMR and memristive properties in a single RS device [33–35]. In this work, we fabricate the RS device using  $\text{La}_{0.5}\text{Ca}_{0.5}\text{MnO}_{3-\delta}$  (LCMO) epitaxial films, and we show that the electric pulses result in local confined oxygen vacancies layer near the metal-oxide interface, which effectively decreases the magnetic fields for the AFM-CO state melting not only in the interfacial memristive domain, but also in the common pristine domains. We also find that after the AFM-CO state melting, the thermal induced metal-insulator transition displays a clear difference between the memristive states and the original resistive state.

II. EXPERIMENT

The employed LCMO films with thickness  $t \sim 200$  nm were grown onto single crystal  $\text{SrTiO}_3$ (STO)(001)( $5 \times 5 \text{ mm}^2$ ) by pulse laser deposition at  $850^\circ\text{C}$  under 0.4 mbar of oxygen partial pressure, and annealed *in situ* at  $900^\circ\text{C}$  under 1 bar oxygen atmosphere. The presence of single isolated and clustered oxygen vacancies in these half-doped manganese films has been confirmed and should arise from a high-temperature ( $850^\circ\text{C}$ – $900^\circ\text{C}$ ) growth process and a cooperative strain effect [36,37]. Note that, for the RS devices based on manganites such as  $\text{Pr}_{0.7}\text{Ca}_{0.3}\text{MnO}_3$  and  $\text{La}_{0.7}\text{Ca}_{0.3}\text{MnO}_3$ , it has been verified that the redox reaction of an active electrode (Al, Ti, W) at the metal-oxide interface leads to the positive bipolar RS, in which the resistance decreases by applying negative electric pulse (defined as the current flows out from the manganite film through the metal electrode) [38]. In

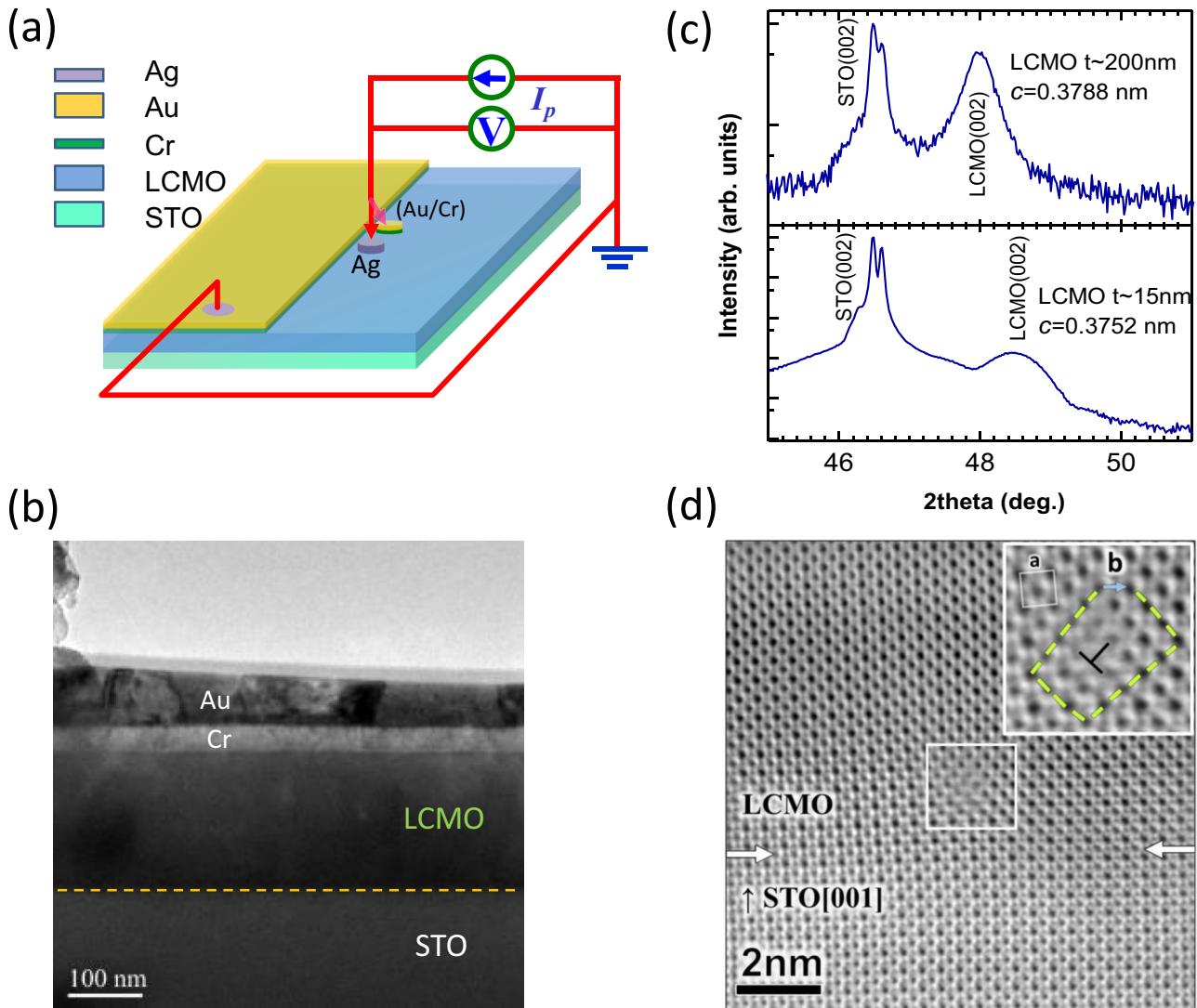


FIG. 1. (a) Schematic of the Ag-RS device (Ag/LCMO/Cr/Au) and the reference device Au-Ref (Au/Cr/LCMO/Cr/Au) fabricated on a single LCMO film grown on STO(001). (b) TEM image for the local cross-section structure of the RS device with the common Cr/Au electrode. (c) The  $\theta \sim 2\theta$  x-ray diffraction for the LCMO films with thickness ( $t$ ) of  $\sim 200$  and 15 nm. (d) The high-resolution cross-section STEM image for the LCMO film ( $t \sim 200$  nm) grown onto STO(001). The inset illustrates a pseudocubic unit cell and a Burgers circuit around the misfit dislocation core at the LCMO-STO interface.

contrast, when a noble metal (Ag, Pt) is used as the work electrode, the generation and annihilation process of oxygen vacancies at the metal-oxide interface results in negative bipolar RS, in which the resistance increases by applying negative electric pulse [38]. Because the latter frame ensures electromigration of oxygen vacancies *within the films*, our RS device adopts the silver pad as the work electrode. As schematically shown in Fig. 1(a), we fabricate the planar RS device [Ag/LCMO/(Cr/Au), abbreviated as Ag-RS] and the reference none-RS device [(Au/Cr)/LCMO/(Cr/Au), abbreviated as Au-Ref], which have the independent close-by Ag contact ( $\sim 0.25 \times 0.5 \text{ mm}^2$ ) and the small (Cr/Au) contact similar to Ag, while both share the same LCMO film and the same large (Cr/Au) contact ( $\sim 2.5 \times 5 \text{ mm}^2$ ). The small Ag and (Cr/Au) electrodes space  $\sim 0.2 \text{ mm}$  apart from the large common (Cr/Au) electrode. With the latter metal contact, the cross-section structure of the devices was illustrated by a low magnification transmission electron microscopy (TEM) image [see Fig. 1(b)]. The Ag electrode was prepared by point contact printing and curing of high-quality silver-filled epoxy adhesive (H20E). The (Cr/Au) electrodes were deposited onto the film surface using electron beam evaporation with a shadow mask. It is noteworthy that the growth of the seeding Cr layer ( $t \sim 35 \text{ nm}$ ) before the top Au film ( $t \sim 65 \text{ nm}$ ) deposition is to obtain an Ohmic contact to the LCMO film.

The x-ray diffraction (XRD) was performed using Rigaku and Philips x-ray diffractometers with Cu  $K\alpha$  radiation. The scanning transmission electron microscopy (STEM) was carried out using a JEOL 2100F transmission electron microscope operated at 200 keV. The effective probe size was defined to be  $\sim 0.9 \text{ \AA}$  at an incident angle of 25 mrad. The TEM characterization with selected area electron diffraction were carried out on a Philips CM200 transmission electron microscope equipped with a field-emission gun, operated at an acceleration voltage of 200 kV. The thermomagnetization curve ( $M$ - $T$ ) was measured by a Quantum Design SQUID magnetometer. The impedance spectroscopy measurements were performed at room temperature using a Solartron SI1260 impedance analyzer with a fixed ac signal of 25 mV and the scanning frequency from 7 Hz up to 8 MHz. The electrical transport was carried out on a physical property measurement system (PPMS, Quantum Design). The current pulses with each pulse duration of 10 ms were injected through the Ag contact with the large (Cr/Au) electrode being grounded. The resistance for the two terminal devices was measured with a small probing current of  $10 \mu\text{A}$ . The magnetic field ranging from 0 to 7 T was applied along [100] in the film plane.

### III. RESULTS AND DISCUSSION

The XRD in  $\theta \sim 2\theta$  scan shows only pairs of (00l) reflections from the film and the STO substrate [Fig. 1(c)], indicating a pure perovskite phase in textured growth. The film out-of-plane lattice constant ( $c = 3.788 \text{ \AA}$ ) is less than the pseudocubic value ( $a \sim 3.83 \text{ \AA}$ ) of the bulk LCMO [39], but a bit larger than that ( $c = 3.752 \text{ \AA}$ ) for the ultrathin LCMO film ( $t = 15 \text{ nm}$ ) which was grown at the same condition and undergoes a partial strain relaxation [36]. Aside from revealing an epitaxial growth, the STEM observation shows misfit dislocations at

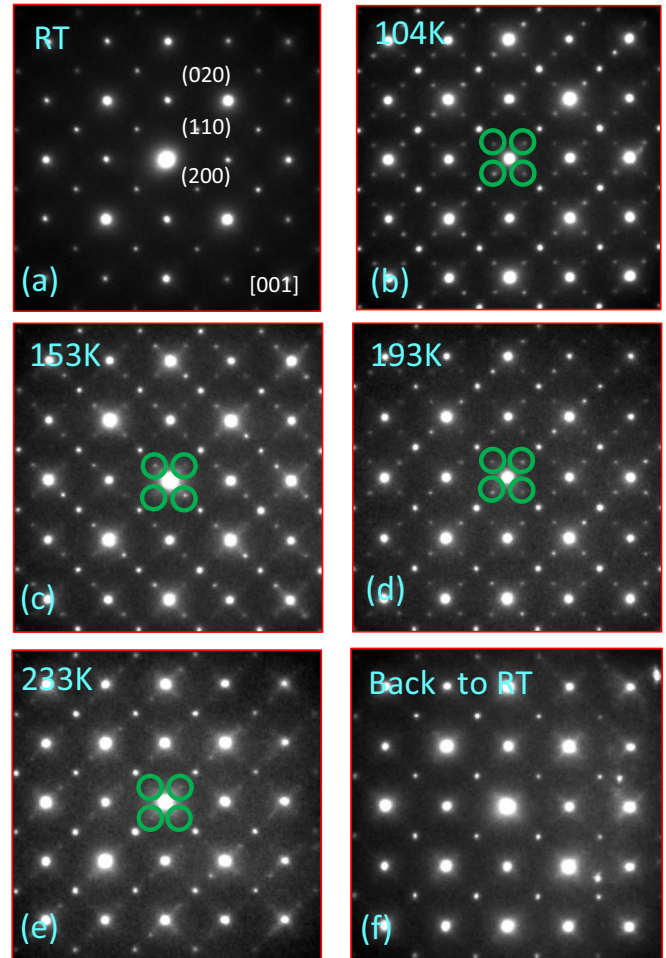


FIG. 2. The selected area electron diffraction pattern first obtained at room temperature (RT) (a), and then at 104 K (b), 153 K (c), 193 K (d), 233 K (e), and back to RT (f). The green circles denote the emergent CO diffractions with  $\mathbf{q} = \frac{2\pi}{a}(\frac{1}{2}, 0, 0)$ .

the LCMO-STO interface [Fig. 1(d)], thus verifying a partial strain relaxation due to the lattice mismatch between LCMO and STO ( $a = 3.905 \text{ \AA}$ ). For bulk LCMO, there first emerges the CO state with an onset temperature ( $T_{\text{CO}}$ ) about 265 K, and then the AFM-CO state around 160 K ( $T_{\text{AFM}}$ ) upon cooling [3,18,40,41]. To unravel the CO state in the LCMO film, the TEM measurements with selected area electron diffraction were performed from 104 to 300 K. As shown by the superstructure diffractions of a wave vector  $\mathbf{q} = \frac{2\pi}{a}(\frac{1}{2}, 0, 0)$ , we find that the LCMO film of a strain relaxation does retain the CO state with  $T_{\text{CO}}$  between 233 and 300 K [see Figs. 2(a)–2(f)]. Figure 3 shows the thermomagnetization curves ( $M$ - $T$ ) of the LCMO film measured at a magnetic field of 1 kOe. The field-cooled (FC)  $M$ - $T$  curve is somewhat FM-like. However, the saturated magnetic moment of only  $\sim 0.12 \mu_B/\text{Mn}$  is rather weak compared to that of a FM manganite in the same magnetic field [1]. Furthermore, the  $dM/dT$  vs  $T$  curve shows a global minimum at  $\sim 168 \text{ K}$ , which matches well with the  $T_{\text{AFM}}$  in bulk LCMO. These facts suggest that the weak FM-like components should arise from the oxygen vacancies induced FM clusters which are randomly dispersed in the retained AFM-CO matrix [2].

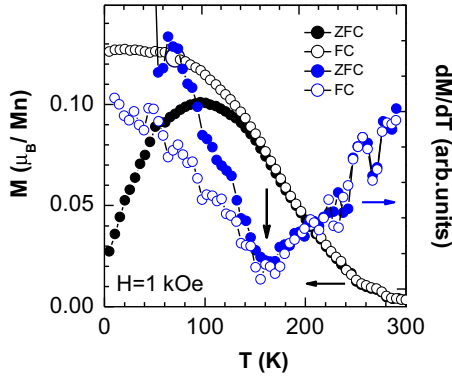


FIG. 3. The magnetization vs temperature ( $M$ - $T$ ) curves measured in warming for the LCMO film with  $H = 1000$  Oe after zero field cooled (ZFC) and field cooled (FC) to 5 K, and the corresponding  $dM/dT$  vs  $T$ , for which the vertical arrow indicates the global minimum at  $T_{AFM} \sim 168$  K.

In our previous work, the forming-free RS in the Ag-RS device has been preliminarily studied at room temperature with attention to the correlation between the RS evolution and the configuration of oxygen vacancies [37]. For the semiconducting LCMO film of clustered oxygen vacancies, the magnitude of electrical pulse for RS should increase markedly with decreasing temperature. We thereby still start from the room-temperature RS in the Ag-RS device but with more in-depth assessments for revealing how the AFM-CO state melts differently with the ambient tuning of oxygen vacancies. To pursue an even more prominent RS, we employ the current pulses with magnitude of  $I_p = \pm 50$  mA which is larger than the threshold  $I_p = \pm 30$  mA for an abrupt RS [37]. As shown in Figs. 4(a) and 4(b), there exhibits the abrupt negative bipolar RS [i.e., switching promptly into the high resistive (HR)/low resistive (LR) states under negative/positive pulses, respectively], which at first excludes the redox-based RS mechanism. Moreover, both the HR and LR profiles remain almost constant over the endurance test, while keeping the RS ratio ( $R_{HR}/R_{LR} \sim 9$ ) more than twice that with current pulses of  $I_p = \pm 30$  mA [37]. Although the present pulses employ a magnitude of 50 mA, the Joule heating effect can be still neglected in evaluating the RS behavior, as otherwise for the semiconducting LCMO, at least the HR profile should have been apparently decayed with increasing the switch cycles and in turn the device temperature. We also note that the pivotal silver electrode does not show any deformation or delamination after the endurance measurements. All these facts verify the reproducible RS events, which are essential to our proposed controlling paradigm as the electromigration of oxygen vacancies can be realized in a repeated manner.

In Fig. 4(c) we show the  $I$ - $V$  characteristics of the Ag-RS and Au-Ref devices measured at 300 K. Owing to both the Ohmic contacts (Au/Cr) to LCMO, the non-RS device (Au-Ref) displays a linear  $I$ - $V$  dependence without any hysteresis, thus protecting a pristine resistive (PR) state of the LCMO film. In contrast, the Ag-RS device exhibits a counterclockwise  $I$ - $V$  hysteresis loop, which is compatible with the negative bipolar RS shown in Figs. 4(a) and 4(b), and meanwhile, resembles very much the  $I$ - $V$  profile in the memristive devices based

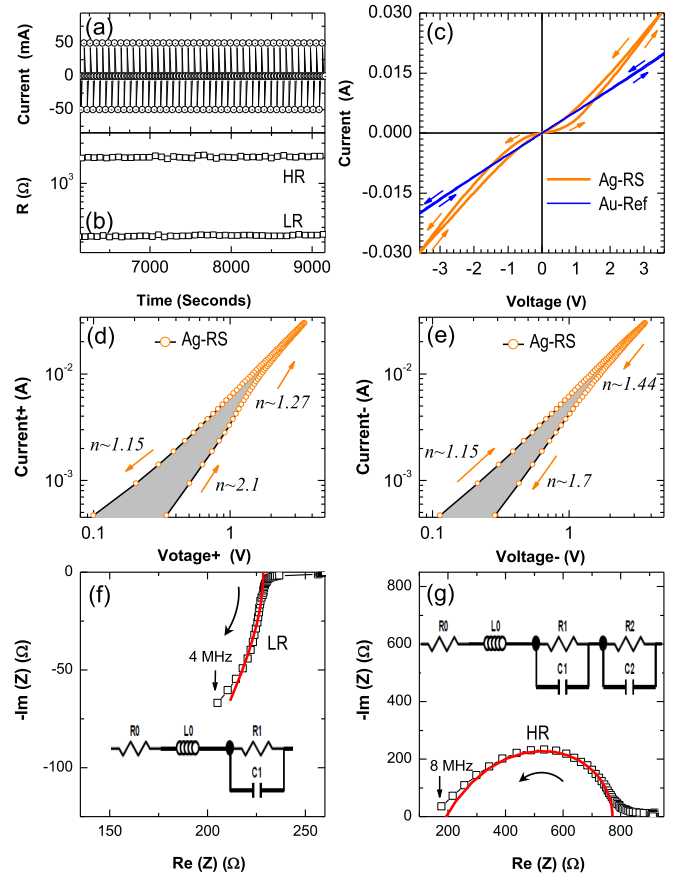


FIG. 4. (a), (b) The endurance characteristics of the RS under bipolar electric pulsings of  $I_p = \pm 50$  mA at 300 K. The two-terminal resistance was measured only once just after each current pulse. (c) The  $I$ - $V$  curves of the Ag-RS device and the Au-Ref device measured at 300 K with current compliance set to 30 mA. The  $I$ - $V$  curves for the Ag-RS device are also plotted separately for the positive bias (d) and the negative (e) bias on double-logarithmic scales, where the slope  $n = d \log I / d \log V$  is marked in different bias regions. (f), (g) Nyquist plots of the impedance spectra taken from the LR state (f) and the HR state (g) obtained by bipolar electric pulsing of  $I_p = \pm 30$  mA at room temperature. The arrows in (c)–(e) denote the current sweeping direction. In (f) and (g), the solid lines in red are the fits to the corresponding equivalent circuit models shown in the insets, while the curved arrows denote the direction of increasing frequency.

on gadolinia-doped ceria of clustered oxygen vacancies [42]. Figures 4(d) and 4(e) replot the  $I$ - $V$  curves of the Ag-RS device in logarithmic scales for the positive- and negative-bias regions, respectively. In the same low-voltage region, the LR state shows a relation of  $I \propto V^{1.15}$  for both the current sweeping directions, whereas the HR state shows  $I \propto V^{2.1}$  and  $I \propto V^{1.7}$  for the forward and backward current sweeping, respectively. The asymmetry in the slope  $n$  ( $n = d \log I / d \log V$ ) and the shaded  $I$ - $V$  hysteresis area between the positive and negative bias indicate a Schottky barrier between the Ag electrode and the LCMO film [43], while for the HR state, its  $I$ - $V$  response close to  $I \propto V^2$  implies a space-charge-limited-current (SCLC) conduction which should arise from the electrotrapped oxygen vacancies near the Ag-LCMO interface [43–45].

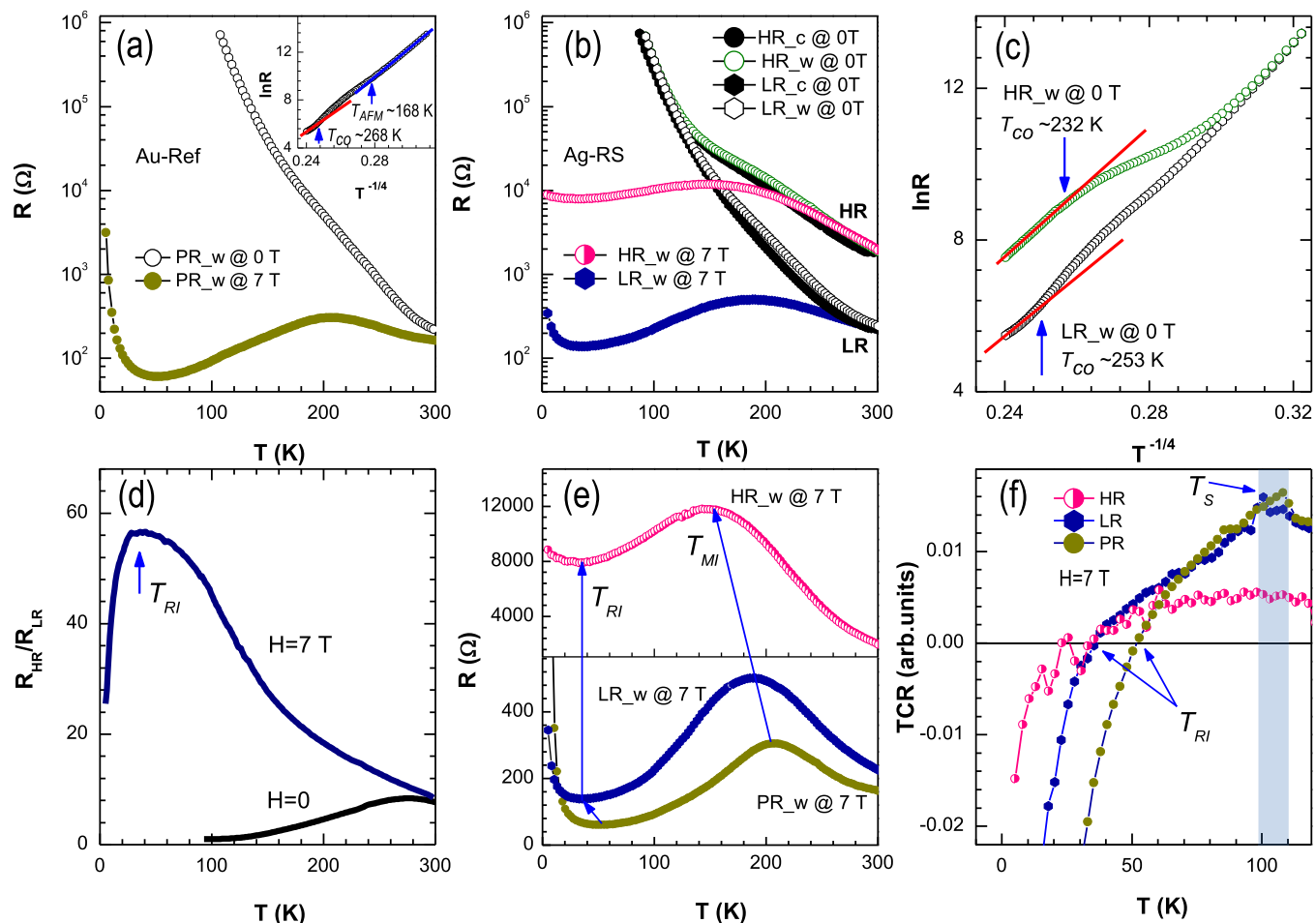


FIG. 5. Temperature dependence of resistance in the Au-Ref device (a) and the Ag-RS device (b) at  $H = 0$  and 7 T. The subscripts “c” and “w” in the labels of HR<sub>c/w</sub> and LR<sub>c/w</sub> denote the measurements in cooling and warming, respectively. The inset of (a) shows the linear fitting of the RT data for the PR state based on the VRH theorem, while the VRH fitting for the LR and HR states are shown in (c). The arrows indicate  $T_{CO}$  and  $T_{AFM}$ . (d) The temperature dependence of  $R_{HR}/R_{LR}$  ratio for the Ag-RS device, and the arrow indicates  $T_{RI}$ . (e) To compare the magnetoresistive states, the RT curves at  $H = 7$  T shown in (a) and (b) are replotted on a linear scale, and the arrows indicate  $T_{MI}$  and  $T_{RI}$ . (f) The calculated TCR =  $d(\ln R)/dT$  vs  $T$  in arbitrary units for the different resistive states at  $H = 7$  T. The arrows denote  $T_{RI}$  and  $T_S$ , while the vertical bar in light blue denotes the STO structural transition region around 105 K.

To better characterize the interface-type RS, we perform impedance spectroscopy measurements in the HR and LR states. As shown in Figs. 4(f) and 4(g), the impedance spectra of real and imaginary parts are plotted in the Nyquist diagram ( $-Z''$  vs  $Z'$ ). Unlike an arclike response shown at the fourth quadrant in the LR state, a distorted semicircle is shown at the first quadrant in the HR state, indicating clearly different electrical properties of these two resistive states. Using ZVIEW software, we find that the impedance data for the LR state can be largely described by an equivalent circuit model consisting of a serial  $R_0/L_0$  ( $0.5 \Omega/10 \mu\text{L}$ ) connection and a parallel  $R_1/C_1$  ( $228 \Omega/99 \text{ pF}$ ) combination, where  $R$ ,  $L$ , and  $C$  represent the resistor, inductor, and capacitor, respectively. As for the HR state, aside from a serial  $R_0/L_0$  ( $1 \Omega/6.5 \mu\text{L}$ ) connection and a parallel  $R_1/C_1$  ( $200 \Omega/155 \text{ pF}$ ) connection, the impedance fitting does require one more parallel  $R_2/C_2$  ( $570 \Omega/62 \text{ pF}$ ) combination. Noting the Ohmic contact between (Au/Cr) and LCMO and the quasi-Ohmic conduction in the LR state, the close  $R_1$  response in both cases should mainly stem from a bulklike contribution in the film device,

while  $C_2 < C_1$  in the HR state suggests that the additional capacitive contribution ( $C_2$ ) should come from the interface layer between Ag and LCMO, which is in good agreement with the SCLC conduction due to the local electromigration of oxygen vacancies.

After accomplishing the RS characterization at room temperature, we then focus on the AFM-CO state melting in the different resistive states. First, we measure the temperature-dependent resistance ( $R$ - $T$ ) of the reference PR state which is protected in the reference device by the double Ohmic Au/Cr-LCMO interfaces. As shown in Fig. 5(a), upon cooling at zero magnetic field ( $H = 0$  T), a bulklike insulating behavior exhibits with two consecutive resistance ramps when entering the CO state at  $T_{CO} \sim 268$  K and then the cooperative AFM-CO state at  $T_{AFM} \sim 168$  K. Both  $T_{CO}$  and  $T_{AFM}$  can be concretely defined through the  $R$ - $T$  data fitting based on the variable range hopping (VRH) theorem [2] [see the inset of Fig. 5(a)], and they are also consistent with the aforementioned TEM and  $M$ - $T$  measurements, respectively. As a magnetic field of 7 T is applied, the resistance was found to be suppressed by several

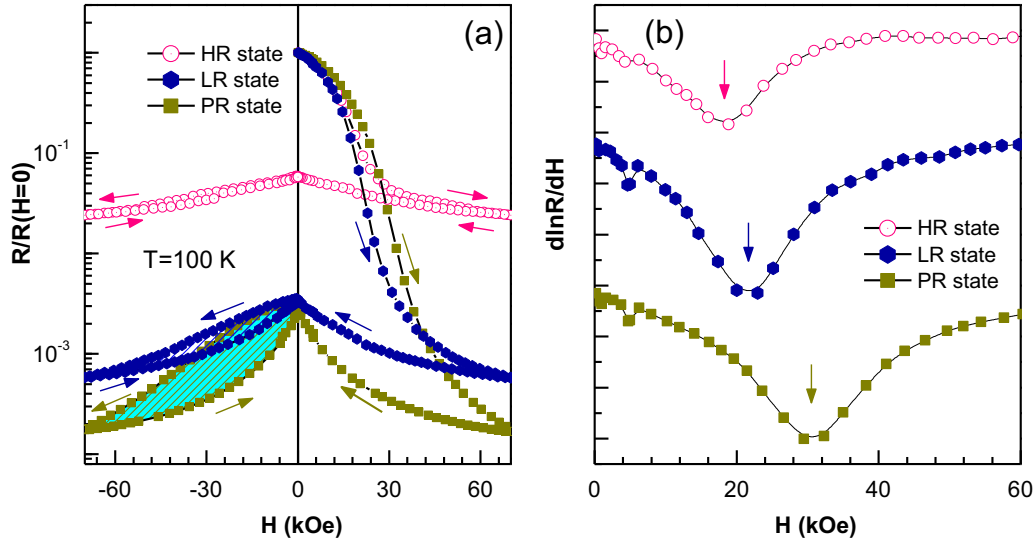


FIG. 6. (a) Resistance vs magnetic fields ( $R$ - $H$ ) for the different resistive states measured at 100 K. The arrows denote the magnetic field sweeping direction. (b) As denoted by the vertical arrows, the minimum in  $d(\ln R)/dH$  for the initial  $R$ - $H$  curve indicates the critical magnetic field ( $H_c$ ) for the AFM-CO state melting.

orders of magnitude, in particular below  $T_{AFM}$ , indicating a melting of the AFM-CO state. Furthermore, the  $R$ - $T$  curve at  $H = 7$  T shows a metal-insulator transition peak at  $T_{MI} \sim 207$  K and another minor reentrant insulating below  $T_{RI} \sim 52$  K [see also Fig. 5(e)]. In Fig. 5(f), we show the temperature dependence of the thermal coefficient of resistance (TCR, defined by  $TCR = d \ln R / dT$  at  $H = 7$  T) for the PR state. Aside from the  $T_{RI}$  with  $TCR \sim 0$ , the TCR curve shows a cusp around  $T_s \sim 105$  K, which coincides with the cubic-to-tetragonal structural transition in the STO substrate. It is noteworthy that the similar magnetic and transport anomalies at  $\sim 105$  K were also observed in other metallic manganite films epitaxially grown on STO single crystals, such as  $La_{0.65}Ca_{0.35}MnO_3$ ,  $Nd_{0.55}Sr_{0.45}MnO_3$ , and  $La_{1-x}Sr_xMnO_3$  ( $x = 0.2, 0.3$ , and  $0.47$ ) [46–48]. Moreover, STO is known to be nonmagnetic and highly insulating, and such a 105-K transition has not been owned by the bulk LCMO and the aforementioned bulk manganites. Hence, we attribute the present TCR anomaly in the charge order melted state to a coupling between the charge carriers in the LCMO and the phonon softening that occurs in STO around the 105-K structural transition [47,48]. In other words, because the LCMO film is mechanically constrained to the STO single-crystal substrate, the  $TiO_6$  octahedra rotations along the  $c$  axis should couple to the  $MnO_6$  ones, thereby inducing both static and dynamic changes in their configuration.

Due to the nonvolatile nature of the memristive states, the distribution of oxygen vacancies electrotailed at the metal-oxide interface should be statically fixed after switching off the electric pulses. To minimize the possible back-diffusion of oxygen vacancies, we commence the  $R$ - $T$  measurements ( $T: 300$  K  $\rightarrow$  5 K  $\rightarrow$  300 K) of the Ag-RS device immediately once setting the LR and HR states at 300 K by the current pulses of  $I_p = \pm 50$  mA, respectively. As displayed in Fig. 5(b), both the LR and HR states exhibit an insulating behavior at zero magnetic field but, upon cooling, the difference between  $R_{HR}$  and  $R_{LR}$  begins to be clearly suppressed below  $T_{CO} \sim$

268 K, and they become nearly coincident ( $R_{HR}/R_{LR} \sim 1$ ) below 100 K [Fig. 5(d)]. Note that, after the thermal cycle 300 K  $\rightarrow$  5 K  $\rightarrow$  300 K which takes about  $9 \times 10^3$  s, both  $R_{HR}$  and  $R_{LR}$  return to their corresponding values initially electroset at 300 K. This fact suggests that the reduced  $R_{HR}/R_{LR}$  upon cooling should not be attributed to a resistance relaxation effect which could occur due to oxygen vacancies and/or Ag diffusions [26]. On the other hand, when applying a magnetic field of 7 T, there similarly occurs field-induced insulator to metal transitions, which reparate the LR and HR states (with increasing  $R_{HR}/R_{LR}$  up to 56), and meanwhile unravels the following differences between the three (LR, HR, and PR) states: (i) The metal-insulator transition peak that is well defined at  $T_{MI}$  in each  $R$ - $T$  curve shows a relation  $T_{MI}^{HR}(148$  K)  $<$   $T_{MI}^{LR}(189$  K)  $<$   $T_{MI}^{PR}(207$  K) [see Fig. 5(e)]. (ii) Compared to the PR state, the reentrant insulating behavior is suppressed to lower temperatures in the LR and HR states with a relation  $T_{RI}^{HR}(35$  K)  $\sim$   $T_{RI}^{LR} <$   $T_{RI}^{PR}(52$  K) [Fig. 5(e)]. (iii) The TCR peak due to the STO  $\sim 105$  K structure phase transition is still visible in the LR state, albeit it is absent in the HR state [Fig. 5(f)].

For an in-depth view of the AFM-CO state melting, we measure the magnetic field dependence of resistance change ( $R$ - $H$ ) in these three resistive states at 100 K. As shown in Fig. 6(a), all the first-order AFM-FM transition due to the charge order melting manifests as a sharp drop of resistance at a critical magnetic field ( $H_c$ ), which can be defined from the  $d(\ln R)/dH$  minimum [Fig. 6(b)]. For the PR state,  $H_c \sim 31$  kOe. For the Ag-RS device in the LR and HR states,  $H_c$  has been reduced to 21 and 19 kOe, respectively. Moreover, after the initial magnetic field sweeping to 7 T and then back to zero, the hysteresis area enclosed by the subsequent field sweeping ( $H = 0 \rightarrow -7$  T  $\rightarrow 0$ ) becomes progressively smaller from the PR state to the LR state, and then the HR state.

Below we attempt to present a unified picture to describe the control of the AFM-CO state melting process. Notably first, the planar Ag-RS device was designed to have the (Cr/Au) Ohmic

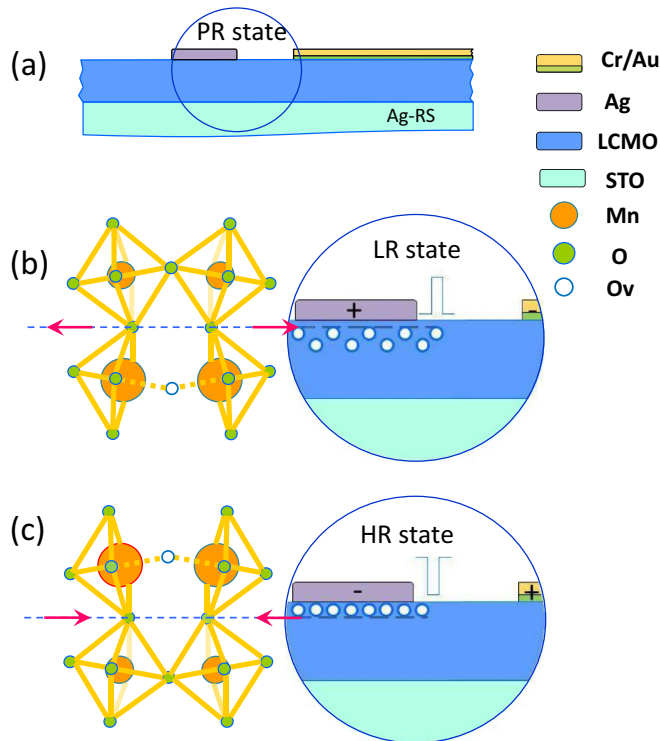


FIG. 7. Schematic model of the Ag-RS device cross section in the PR state (a) and the memristive states (b), (c). In the PR state (a), the oxygen vacancies (not shown) are randomly dispersed in the LCMO film. In the LR state (b), the focused circle depicts the local forming of 2D-like layers of little oxygen vacancies at the Ag-LCMO interface, while the adjacent deeper region is driven to have oxygen vacancies *in gradient dilution* along the  $c$  axis. In the HR state (c), the focused circle depicts the forming of local compacted 2D-like layers of oxygen vacancies at the Ag-LCMO interface, while leaving little oxygen vacancies in the adjacent deeper region. The associated local dynamic tensile or compressive strain due to the chemical expansion effect are illustrated with oxygen vacancies repelled away from or attracted to the Ag-LCMO interface in the left of (b) and (c), respectively. Only Mn-O octahedra in the perovskite are shown for clarity. The dashed lines in the left and right panels of (b) and (c) indicate the local separation interface between the oxygen vacancies rich and poor layers formed in the RS. The arrows along the separation interface denote the direction for the dynamic tensile and compressive strain (see also Ref. 56).

contacting area  $\sim 10^2$  times larger than that of the Ag electrode. Owing to such a design with the Schottky barrier between Ag and LCMO, the electric pulsing confines an intensified electric field near the small electrode (Ag), and a minimized one near the large electrode (Cr/Au) [49,50]. In the PR state, the oxygen vacancies are *randomly dispersed* in the LCMO film [37]. To set the LR state [see Fig. 7(b)], the applied positive electric pulse repels the oxygen vacancies away from the Ag electrode, forming two-dimensional- (2D-) like layers of little oxygen vacancies at the Ag-LCMO interface, while the adjacent deeper region is driven to have oxygen vacancies *in gradient dilution* along the  $c$  axis. This local electromigration of oxygen vacancies still allows the coupling between the LCMO and the phonon softening that occurs in STO around the 105-K transition, thus inducing the TCR anomaly as that in the PR

state. As to set the HR state [see Fig. 7(c)], the applied negative pulse attracts the oxygen vacancies towards the Ag electrode, forming compact 2D-like layers of oxygen vacancies at the Ag-LCMO interface, while leaving little oxygen vacancies in the adjacent deeper region. This local coherent distribution of oxygen vacancies, which is evidenced by the SCLC conduction and the additional capacitive contribution of  $C_2$ , interrupts the coupling between the LCMO and the  $\sim 105$ -K phonon softening in STO, thus erasing the TCR anomaly in the HR state. In both cases, the weak electric field in the common domains of the RS device (due to leaving far away from the Ag-LCMO interface), results in little motion of oxygen vacancies, thus reserving almost the same CO properties as that for the PR state. In light of this picture, the overlapped  $R_{HR}$  and  $R_{LR}$  at low temperatures and  $H = 0$  T should arise from the pristine charge ordering in the common domain which becomes dominated in the device resistance below  $T_{AFM} \sim 168$  K. By contrast, the observed resistive states (HR, LR) of a large difference at higher temperatures with  $H = 0$  T should be attributed to the memristive domain close to the Ag-LCMO interface [51]. Note that the resistance gap between the HR and LR states is still remarkable in the high-temperature  $R$ - $T$  curve at  $H = 0$  T, the onset CO temperatures for the *interfacial* LR and HR states can be validly extracted by the VRH theorem fitting, which results in a relation  $T_{CO}^{HR}(232 \text{ K}) < T_{CO}^{LR}(253 \text{ K}) < T_{CO}^{PR}(268 \text{ K})$  [see Fig. 5(c)].

In general, the physical properties difference between the HR and LR states in RS devices can be ascribed to the charge carriers doping from the electromigrated oxygen vacancies. Nevertheless, if only considering this effect, the LR state of evacuated oxygen vacancies at the Ag-LCMO interface should have an enhanced CO state with  $T_{CO}$  higher than that of the PR state of dispersed oxygen vacancies, which is in fact contrary to the observation [52,53]. We note that, although the present electrical pulsing in the HR and LR cases involves about the same amount of oxygen vacancies, their different layer profiles of oxygen vacancies would cause different chemical expansion, an effect due to the electrostatic repulsion from the surrounding cations of reduced valence state and increased ionic radius [54–56]. In the HR scenario, the coherent 2D-like layers of oxygen vacancies at the Ag-LCMO interface would be imposed by a large in-plane biaxial compressive strain from the underneath domain of little oxygen vacancies, thus markedly suppressing both  $T_{CO}$  and  $T_{MI}$  [36,57,58]. In the LR scenario, the 2D-like layers of little oxygen vacancies at the Ag-LCMO interface bear a minor tensile strain from the underneath layers of oxygen vacancies in a gradient dilution, thus just mildly decreasing  $T_{CO}$  and  $T_{MI}$ , as compared to the PR state.

Since the temperature-dependent resistance in the HR and LR states become almost equal at 100 K and  $H = 0$  T, the critical magnetic fields  $H_c$  known from the  $R$ - $H$  measurements should reflect the global AFM-CO state melting in the common domain of the RS device. At first glance, the  $H_c$ 's for the pristine CO state melting should be the same in all the cases. However, the concrete relation is  $H_c^{HR} < H_c^{LR} < H_c^{PR}$ . In fact, the reduced  $H_c$  in the memristive states can be also seen from the  $T_{RIS}$  in their  $R$ - $T$  curves at  $H = 7$  T. Note that  $H_c$  generally increases upon cooling [59]. As shown in Fig. 5(e), the low-temperature reentrant insulating behavior at  $H = 7$  T

in the PR state implies that the  $H_c$  for a complete CO state melting needs to be larger than 7 T below  $T_{RI} = 52$  K. In contrast, the reentrant insulating behavior at  $H = 7$  T in the LR and HR states was suppressed with  $T_{RI}$  reduced to 32 K, indicating a suppressed  $H_c$  ( $< 7$  T) at least for the temperature window from 32 to 52 K in these two memristive states. Furthermore, it can be seen that the relation  $H_c^{HR} < H_c^{LR} < H_c^{PR}$  actually follows the one  $T_{CO}^{HR} \sim (232 \text{ K}) < T_{CO}^{LR} \sim (253 \text{ K}) < T_{CO}^{PR} \sim (268 \text{ K})$ . Note that the more weakened CO state, the less  $H_c$  required for CO state melting in half-doped manganites [18] and, in fact, the obtained  $T_{CO}^{HR,LR}$  pertain to the interfacial memristive states. The above comparison thus likely reveals that the local premelting of the AFM-CO state in the interface memristive domains promotes the pristine AFM-CO state melting in the common domain of the RS device. Compared to the oxygen vacancies dispersed in the PR state, the formed layers of oxygen vacancies in the LR and HR states locally alter the structural distortion, which consequently weakens the AFM-CO state and enables the FM clusters separation with an *in-plane* magnetic anisotropy that easily triggers the pristine AFM-CO state melting at a reduced  $H_c$  [18]. For the LR case, its  $H_c$  appears slightly higher than that in the HR case. This could be due to the layers of oxygen vacancies in a gradient dilution for the former case, which leads to a minor suppression of the in-plane magnetic anisotropy of the FM clusters embedded in the AFM-CO matrix. On the other hand, the  $R$ - $H$  response after the initial resistance drop in the RS device should mainly associate with the magnetic-field-induced FM state near the Ag-LCMO interface. For the PR state, the hysteresis enclosed by the subsequent field sweeping after the initial AFM-CO state melting implies that the magnetic-field-induced FM state is not stable with zero magnetic field, in other words, there exists a reverse FM-AFM transition once the magnetic field is decreased to zero [59]. The systematically suppressed hysteresis area from the PR state to the LR and HR states indicates that the oxygen vacancies in more coherent layers should be more capable to trap the magnetic-field-induced FM state.

#### IV. CONCLUSION

In conclusion, we demonstrate that an *in situ* local tailoring of oxygen vacancies based on a memristive switch provides an avenue to control the AFM-CO state melting in CMR manganites. This dynamic control can be naturally expanded to the strongly correlated behavior in other transition metal oxides, such as the cuprates and the recently focused iridates. On the other hand, as a mutual benefit, the strong correlation behavior could be served as interior probes for searching an efficient control of the RS properties. For example, a coherent understanding of the phase transition temperatures and the chemical expansion effect due to the layer distribution of oxygen vacancies may shed light on achieving stable memristive states through designing some specific fish-hook-like structure against the back-diffusion of oxygen vacancies towards or away from the metal-oxide interface at zero electric bias. We believe that the pivotal roles of functional oxygen vacancies and their dynamics deserve further investigations, which should not only be fundamentally fruitful but also pave the way for novel oxide electronics.

#### ACKNOWLEDGMENTS

This work was supported by National Natural Science Foundation of China (Contracts No. 10774173, No. 11174353, and No. 11474342), National Program on Key Basic Research Project, National Natural Science Foundation of innovation research group project, the Strategic Priority Research Program of the Chinese Academy of Sciences, National Science Fund for Excellent Young Scholars, and National Natural Science Funds for Distinguished Young Scholar of China. Z.-H.W. thanks Dr. G. Logvenov, Dr. O. I. Lebedev, M. Schulz, S. Schmid, B. Lemke, and B. Stuhlhofer for help and discussions, and the Max-Planck-Gesellschaft for financial support during his three-month revisiting at MPI-FKF. Z.-H.W. is also grateful to the anonymous reviewers for their helpful comments and suggestions.

- 
- [1] M. B. Salamon and M. Jaime, *Rev. Mod. Phys.* **73**, 583 (2001).
  - [2] Y. Tokura, *Rep. Prog. Phys.* **69**, 797 (2006).
  - [3] E. O. Wohlan and W. C. Koehler, *Phys. Rev.* **100**, 545 (1955).
  - [4] J. B. Goodenough, *Phys. Rev.* **100**, 564 (1955).
  - [5] J. C. Loudon, N. D. Mathur, and P. A. Midgley, *Nature (London)* **420**, 797 (2002).
  - [6] G. C. Milward, M. J. Calderón, and P. B. Littlewood, *Nature (London)* **433**, 607 (2005).
  - [7] F. Ye, J. A. Fernandez-Baca, P. Dai, J. W. Lynn, H. Kawano-Furukawa, H. Yoshizawa, Y. Tomioka, and Y. Tokura, *Phys. Rev. B* **72**, 212404 (2005).
  - [8] S. Cox, J. Singleton, R. D. McDonald, A. Migliori, and P. B. Littlewood, *Nat. Mater.* **7**, 25 (2008).
  - [9] L. Brey and P. B. Littlewood, *Phys. Rev. Lett.* **95**, 117205 (2005).
  - [10] D. Koumoulis, N. Panopoulos, A. Reyes, M. Fardis, M. Pissas, A. Douvalis, T. Bakas, D. N. Argyriou, and G. Papavassiliou, *Phys. Rev. Lett.* **104**, 077204 (2010).
  - [11] Ch. Jooss, L. Wu, T. Beetz, R. F. Klie, M. Beleggia, M. A. Schofield, S. Schramm, J. Hoffmann, and Y. Zhu, *Proc. Natl. Acad. Sci. USA* **104**, 13597 (2007).
  - [12] T. Ogasawara, K. Tobe, T. Kimura, H. Okamoto, and Y. Tokura, *J. Phys. Soc. Jpn.* **71**, 2380 (2002).
  - [13] Y. Tomioka and Y. Tokura, *Phys. Rev. B* **70**, 014432 (2004).
  - [14] M. Matsubara, T. Ogasawara, Y. Tomimoto, K. Tobe, H. Okamoto, and Y. Tokura, *J. Phys. Soc. Jpn.* **78**, 023707 (2009).
  - [15] H. Matsuzaki, H. Uemura, M. Matsubara, T. Kimura, Y. Tokura, and H. Okamoto, *Phys. Rev. B* **79**, 235131 (2009).
  - [16] H. Yada, Y. Ijiri, H. Uemura, Y. Tomioka, and H. Okamoto, *Phys. Rev. Lett.* **116**, 076402 (2016).
  - [17] E. Dagotto, *Nanoscale Phase Separation and Colossal Magnetoresistance: The Physics of Manganites and Related Compounds* (Springer, New York, 2002).
  - [18] Z.-H. Wang, F. W. Wang, X. Y. Li, G. R. Xiao, W. He, J. Sun, and B. G. Shen, *Adv. Electron. Mater.* **1**, 1500051 (2015).
  - [19] D. A. Muller, N. Nakagawa, A. Ohtomo, J. L. Grazul, and H. Y. Hwang, *Nature (London)* **430**, 657 (2004).

- [20] D. D. Cuong, B. Lee, K. M. Choi, H.-S. Ahn, S. Han, and J. Lee, *Phys. Rev. Lett.* **98**, 115503 (2007).
- [21] N. N. Loshkareva, N. V. Mushnikov, A. V. Korolyov, E. A. Neifeld, and A. M. Balbashov, *Phys. Rev. B* **77**, 052406 (2008).
- [22] A. Sawa, *Mater. Today* **11**, 28 (2008).
- [23] R. Waser, R. Dittmann, G. Staikov, and K. Szot, *Adv. Mater.* **21**, 2632 (2009).
- [24] D. S. Jeong, R. Thomas, R. S. Katiyar, J. F. Scott, H. Kohlstedt, A. Petraru, and C. S. Hwang, *Rep. Prog. Phys.* **75**, 076502 (2012).
- [25] J. J. Yang, D. B. Strukov, and D. R. Stewart, *Nat. Nanotechnol.* **8**, 13 (2013).
- [26] Y. B. Nian, J. Strozier, N. J. Wu, X. Chen, and A. Ignatiev, *Phys. Rev. Lett.* **98**, 146403 (2007).
- [27] Z. B. Yan and J.-M. Liu, *Ann. Phys.* **358**, 206 (2015).
- [28] S. Tang, F. Tesler, F. G. Marlasca, P. Levy, V. Dobrosavljević, and M. Rozenberg, *Phys. Rev. X* **6**, 011028 (2016).
- [29] C. A. F. Vaz, J. Hoffman, Y. Segal, J. W. Reiner, R. D. Grober, Z. Zhang, C. H. Ahn, and F. J. Walker, *Phys. Rev. Lett.* **104**, 127202 (2010).
- [30] D. Yi, J. Liu, S. Okamoto, S. Jagannatha, Y.-C. Chen, P. Yu, Y.-H. Chu, E. Arenholz, and R. Ramesh, *Phys. Rev. Lett.* **111**, 127601 (2013).
- [31] F. A. Cuellar, Y. H. Liu, J. Salafranca, N. Nemes, E. Iborra, G. Sanchez-Santolino, M. Varela, M. G. Hernandez, J. W. Freeland, M. Zhernenkov, M. R. Fitzsimmons, S. Okamoto, S. J. Pennycook, M. Bibes, A. Barthélémy, S. G. E. te Velthuis, Z. Sefrioui, C. Leon, and J. Santamaria, *Nat. Commun.* **5**, 4215 (2014).
- [32] N. P. Lu, P. F. Zhang, Q. H. Zhang, R. M. Qiao, Q. He, H. B. Li, Y. J. Wang, J. W. Guo, D. Zhang, Z. Duan *et al.*, *Nature (London)* **546**, 124 (2017).
- [33] S. Duhaldea, M. Villafuerte, G. Juárez, and S. P. Heluani, *Phys. B (Amsterdam)* **354**, 11 (2004).
- [34] *Thin-Film Metal-Oxides: Fundamentals and Applications in Electronics and Energy*, edited by S. Ramanathan (Springer, Heidelberg, 2010), Chap. 4.
- [35] S. V. Kalinin and N. A. Spaldin, *Science* **341**, 858 (2013).
- [36] Z.-H. Wang, O. I. Lebedev, G. Van Tendeloo, G. Cristiani, and H.-U. Habermeier, *Phys. Rev. B* **77**, 115330 (2008).
- [37] Z.-H. Wang, Y. Yang, L. Gu, H.-U. Habermeier, R. C. Yu, T. Y. Zhao, J. R. Sun, and B. G. Shen, *Nanotechnology* **23**, 265202 (2012).
- [38] R. Yang, X. M. Li, W. D. Yu, X. D. Gao, D. S. Shang, X. J. Liu, X. Cao, Q. Wang, and L. D. Chen, *Appl. Phys. Lett.* **95**, 072105 (2009).
- [39] P. M. Woodward, T. Vogt, D. E. Cox, A. Arulraj, C. N. R. Rao, P. Karen, and A. K. Cheetham, *Chem. Mater.* **10**, 3652 (1998).
- [40] C. H. Chen and S.-W. Cheong, *Phys. Rev. Lett.* **76**, 4042 (1996).
- [41] P. G. Radaelli, D. E. Cox, M. Marezio, and S.-W. Cheong, *Phys. Rev. B* **55**, 3015 (1997).
- [42] R. Schmitt, J. Spring, R. Korobko, and J. L. M. Rupp, *ACS Nano* **11**, 8881 (2017).
- [43] A. Odagawa, H. Sato, I. H. Inoue, H. Akoh, M. Kawasaki, Y. Tokura, T. Kanno, and H. Adachi, *Phys. Rev. B* **70**, 224403 (2004).
- [44] A. Rose, *Phys. Rev.* **97**, 1538 (1955).
- [45] M. A. Lampert, *Phys. Rev.* **103**, 1648 (1956).
- [46] M. Ziese, I. Vrejoiu, A. Setzer, A. Lotnyk, and D. Hesse, *New J. Phys.* **10**, 063024 (2008).
- [47] M. Egilmez, M. M. Saber, I. Fan, K. H. Chow, and J. Jung, *Phys. Rev. B* **78**, 172405 (2008).
- [48] Y. Segal, K. F. Garrity, C. A. F. Vaz, J. D. Hoffman, F. J. Walker, S. Ismail-Beigi, and C. H. Ahn, *Phys. Rev. Lett.* **107**, 105501 (2011).
- [49] Y. W. Xie, J. R. Sun, D. J. Wang, S. Liang, and B. G. Shen, *J. Appl. Phys.* **100**, 033704 (2006).
- [50] Y. Z. Chen, J. L. Zhao, J. R. Sun, N. Pryds, and B. G. Shen, *Appl. Phys. Lett.* **97**, 123102 (2010).
- [51] M. J. Rozenberg, I. H. Inoue, and M. J. Sánchez, *Phys. Rev. Lett.* **92**, 178302 (2004).
- [52] S. V. Trukhanov, N. V. Kasper, I. O. Troyanchuk, M. Tovar, H. Szymczak, and K. Bärnere, *J. Solid Stat. Chem.* **169**, 85 (2002).
- [53] R. Cortés-Gil, L. Ruiz-González, J. M. Alonso, M. García-Hernández, A. Hernando, and J. M. González-Calbet, *Chem. Mater.* **24**, 2519 (2012).
- [54] S. R. Bishop, K. L. Duncan, and E. D. Wachsman, *J. Am. Ceram. Soc.* **93**, 4115 (2010).
- [55] Y. Kuru, M. Usman, G. Cristiani, and H.-U. Habermeier, *J. Cryst. Growth* **312**, 2904 (2010).
- [56] U. Aschauer, R. Pfenninger, S. M. Selbach, T. Grande, and N. A. Spaldin, *Phys. Rev. B* **88**, 054111 (2013).
- [57] Y. Uozu, Y. Wakabayashi, Y. Ogimoto, N. Takubo, H. Tamaru, N. Nagaosa, and K. Miyano, *Phys. Rev. Lett.* **97**, 037202 (2006).
- [58] G. H. Aydogdu, Y. Kuru, and H.-U. Habermeier, *Mater. Sci. Eng. B* **144**, 123 (2007).
- [59] G. Xiao, E. J. McNiff Jr., G. Q. Gong, A. Gupta, C. L. Canedy, and J. Z. Sun, *Phys. Rev. B* **54**, 6073 (1996).